

Nanothermometry-Enabled Intelligent Laser Tissue Soldering


Oscar Cipolato, Lucas Dosnon, Jachym Rosendorf, Sima Sarcevic, Marius Zäch, Alice Bondi, Vaclav Liska, Andrea A. Schlegel, and Inge K. Herrmann*

While often life-saving, surgical resectioning of diseased tissues puts patients at risk for post-operative complications. Sutures and staples are well-accepted and routinely used to reconnect tissues, however, their mechanical mismatch with biological soft tissue and invasiveness contribute to wound healing complications, infections, and post-operative fluid leakage. In principle, laser tissue soldering offers an attractive, minimally-invasive alternative for seamless soft tissue fusion. However, despite encouraging experimental observations, including accelerated healing and lowered infection risk, critical issues related to temperature monitoring and control during soldering and associated complications have prevented their clinical exploitation to date. Here, intelligent laser tissue soldering (iSoldering) with integrated nanothermometry is introduced as a promising yet unexplored approach to overcome the critical shortcomings of laser tissue soldering. It demonstrates that adding thermoplasmonic and nanothermometry nanoparticles to proteinaceous solders enables heat confinement and non-invasive temperature monitoring and control, offering a route to high-performance, leak-tight tissue sealing even at deep tissue sites. The resulting tissue seals exhibit excellent mechanical properties and resistance to chemically-aggressive digestive fluids, including gastrointestinal juice. The iSolder can be readily cut and shaped by surgeons to optimally fit the tissue defect and can even be applied using infrared light from a medically approved light source, hence fulfilling key prerequisites for application in the operating theatre. Overall, iSoldering enables reproducible and well-controlled high-performance tissue sealing, offering new prospects for its clinical exploitation in diverse fields ranging from cardiovascular to visceral and plastic surgery.

1. Introduction

Surgical interventions, while often life-saving, put patients at risk for post-operative complications.^[1] Leak-tight sealing of fluid-containing structures, including blood vessels and organs of the gastrointestinal tract after diseased part resectioning, are pivotal yet technically demanding surgical tasks.^[2,3] While sutures and staples are well-accepted and routinely used to reconnect tissues, their mechanical mismatch with biological soft tissue and invasiveness contribute to wound healing complications, infections, and fluid leakage after surgery.^[4] Leaks and infections can rapidly deteriorate the patient's condition and are significant causes of mortality.^[5] The invasiveness of sutures and staples resulting in foreign body reaction with local inflammation has increased the need to develop adequate alternatives, either as replacements or as suture support materials. Surgical adhesives and glues seem appealing choices^[3,6,7] but also present challenges, including low adhesion (e.g., fibrin-based glues and poly(ethylene glycol), or PEGs), toxicity (e.g., cyanoacrylates^[8]), low chemical stability (fibrin glues are prone to digestion in gastrointestinal fluids^[6,9]), foreign body reactions, and immunogenicity.^[10] Recent work on

O. Cipolato, L. Dosnon, M. Zäch, A. Bondi, I. K. Herrmann
Nanoparticle Systems Engineering Laboratory
Institute of Energy and Process Engineering (IEPE)
Department of Mechanical and Process Engineering (D-MAVT)
ETH Zurich
Zurich 8092, Switzerland
E-mail: ingeh@ethz.ch

 The ORCID identification number(s) for the author(s) of this article can be found under <https://doi.org/10.1002/smt.202300693>

© 2023 The Authors. Small Methods published by Wiley-VCH GmbH.
This is an open access article under the terms of the Creative Commons Attribution-NonCommercial License, which permits use, distribution and reproduction in any medium, provided the original work is properly cited and is not used for commercial purposes.

DOI: 10.1002/smt.202300693

O. Cipolato, L. Dosnon, I. K. Herrmann
Particles Biology Interactions Laboratory
Department of Materials Meet Life
Swiss Federal Laboratories for Materials Science and Technology (Empa)
St. Gallen 9014, Switzerland

J. Rosendorf, S. Sarcevic, V. Liska
Department of Surgery
Faculty of Medicine in Pilsen
Charles University
Pilsen 32300, Czech Republic

J. Rosendorf, S. Sarcevic, V. Liska
Biomedical Center
Faculty of Medicine in Pilsen
Charles University
Pilsen 32300, Czech Republic

hydrogel-based sealants^[3,7,11,12] has reported promising wet tissue adhesion in a variety of scenarios. However, swelling and biocompatibility concerns currently hamper rapid clinical translations of many of these technologies.^[13]

Laser welding and soldering were proposed decades ago as potential wound-closing methods.^[14–16] Laser welding uses laser energy to alter the molecular structure of the joined tissues. The altered molecules in the biological tissue (especially collagen) can form bonds with their neighbors, resulting in tissue joining. Solder materials may be employed to further improve the mechanical properties of the bonding.^[16] Laser tissue soldering is based on the heating of proteinaceous solders by laser energy, which induces cross-linking and tissue adhesion and offers a promising route to seamless and leak-tight tissue fusion. Laser tissue soldering is particularly appealing because it potentially offers excellent bond strength,^[17] lower tissue inflammatory response^[18] compared to suturing or stapling because of the absence of bulky foreign objects, a reduction in scar tissue formation,^[19] and reduced access for microbial pathogens^[20] because of a waterproof seal. Moreover, it can bond delicate tissues that would otherwise be damaged by conventional suturing.^[21] It may also be faster and relatively non-operator-dependent, especially compared with traditional suturing.^[22]

Despite its promising prospects,^[22] laser tissue welding and soldering depend critically on accurate temperature control, the lack of which has hampered its utility and impact so far.^[20] This has caused the technique to remain in the experimental stage, precluding its widespread clinical adoption. Too-low temperatures lead to insufficient cross-linking of the protein solder resulting in poor tissue adhesion, whereas too-high temperatures lead to irreversible tissue damage and delayed healing. Successful soldering obtaining immediate wound closure and firm bonding requires the solder temperature to reach the collagen denaturation temperature, which may vary from 60 to 80 °C for human tissues.^[16,23] Control of the laser irradiation dosimetry and the corresponding temperature rise is crucial to controlling the risk of irreversible tissue damage.

The application of light-absorbing dyes to improve laser absorption localization. A promising approach to tissue laser soldering is based on near-infrared (NIR) lasers which are only weakly absorbed by the biological tissue, in conjunction with indocyanine green (ICG)^[24] absorption in the NIR. In addition to light-absorbing organic dyes, nanoparticle-based alternatives have gained increasing traction as thermoplasmonic agents, as they show several advantages over organic dyes.^[25,26] The light ex-

tingtion spectra of nanomaterials may be tuned throughout the NIR window based on readily adjustable parameters, including nanoparticle size and shape. Selected nanomaterials feature exceptional molar extinction coefficients, some exceeding those of ICG by up to five orders of magnitude, as in the case of gold nanorods (GNRs).^[25] They also exhibit excellent stability in the body even at high irradiation levels and temperatures.

In this context, the combination of NIR-absorbing plasmonic nanoparticles with laser irradiation tuned to their plasmon absorption resonance wavelengths represents a very efficient solution for local solder heating.^[20,27–29] While such nanoparticles have been widely studied for applications in the cancer field, especially for photothermal therapy,^[30] such approaches have scarcely been exploited for wound healing, let alone tissue soldering. Despite the emergence of photoabsorber-augmented soldering more than a decade ago, laser tissue soldering has not established itself in clinics because of substantial difficulties in monitoring the thermal profile of both the heated solder and the underlying tissue,^[17,31] which is a requirement to minimize tissue damage and optimize bonding strength and overall performance.

The prevailing temperature-measurement difficulties are mostly related to the limitations of the tools used, thermal diffusion, and integration into a control system. Actual temperature measurement within a biological environment is challenging. Traditional temperature measurement tools such as thermocouples are invasive and are not applicable when the target is small compared to the sensor size.^[29,32] Alternative non-contact methods, such as infrared thermography, are inherently limited to the surface. Current approaches rely on assumptions about the biological target's opto-thermal characteristics and the irradiation conditions to retrieve temperature profiles, such as the laser parameters and boundary conditions (e.g., based on the bio-heat equation, which is prone to artifacts).^[17,27] Alternatives, such as magnetic resonance imaging (MRI) and ultrasound imaging, may provide direct real-time, non-invasive temperature monitoring within biological tissues during photothermal treatments without numerical post-processing. However, while MRI is unlikely to become a standard tool for monitoring thermal effects during tissue soldering, ultrasound-based temperature detection is contact-based and therefore has limited feasibility. Terahertz imaging^[20] and photoacoustic imaging may soon offer opportunities, but significant further development is needed.^[29]

A possibly powerful and affordable alternative to overcome current limitations is the use of luminescent thermometry,^[33,34] a simple and non-invasive (non-contact) technique based on thermally-induced changes of the emission spectra (e.g., peak position,^[35,36] peak intensity,^[37] lifetime^[38]) of specific nanomaterials to track the temperature evolution.^[37,39] Nanothermometry approaches may be based on ratiometrics. Ratiometrics monitors the intensity ratio between two emission or excitation peaks, which is appealing because its high resistance to environmental interference allows largely matrix- and environment-independent temperature measurements. The fluorescence intensity ratio is independent of local particle concentration and fluctuating excitation intensity, making it a self-referencing, robust approach.^[40] Among the many nanothermometry candidate materials available, lanthanide nanoparticles are particularly promising because of their low matrix dependency, high quantum yields, high biocompatibility, and tailorability to the NIR

A. A. Schlegel
Swiss HPB and Transplant Center
University Hospital Zurich
Zurich 8091, Switzerland

A. A. Schlegel
Fondazione IRCCS Ca' Granda
Ospedale Maggiore Policlinico
Centre of Preclinical Research
Milan 20122, Italy

A. A. Schlegel
Transplantation Center, Digestive Disease and Surgery Institute and
Department of Immunity and Inflammation
Lerner Research Institute, Cleveland Clinic
Cleveland, OH 44106, United States

range. The absolute temperature of lanthanide nanoparticles can be deduced according to the Boltzmann distribution equation based on emission intensity ratio (I_2/I_1) measurements emitting from the thermally coupled energy levels E_1 and E_2 .^[33] Thermally coupled energy-level pairs typically exploited in lanthanide systems include Er^{3+} ($^2\text{H}_{11/2}$ and $^4\text{S}_{3/2}$),^[41] Nd^{3+} ($^4\text{F}_{5/2}$ and $^4\text{F}_{3/2}$)^[42] and Eu^{3+} ($^5\text{D}_1$ and $^5\text{D}_0$).^[33,43]

This study introduces an intelligent soldering approach (called iSoldering) as a technology to overcome the major shortcomings of contemporary wound-closing approaches. iSoldering advances laser tissue soldering by using nanoenhancers (thermoplasmonics and nanothermometers), paving the way to straightforward water-tight tissue sealing even deep inside the tissue. We demonstrate tissue-sparing heat confinement enabled by thermoplasmonics (gold nanorods) and the much more affordable^[44] and equally-performing TiN, along with fluorescence nanothermometry-based, non-invasive temperature monitoring even at depth. Finally, we show the critical performance benefits of iSoldering for several clinically-relevant scenarios, ranging from non-anatomical liver resections to vascular and intestinal anastomoses.

2. Results

2.1. Design and Mechanisms of iSoldering

An ideal tissue-sealing process unifies performance (strong adhesion, cohesion, wound healing promotion, and infection prevention), safety, processability, applicability, and biocompatibility (Figure 1a). We designed iSolder using an albumin base containing 6.5% gelatin and nanoenhancers (thermoplasmonics and nanothermometers), as shown in Figure 1b–e. Concerning the solder base material, there is broad evidence that albumin-based solder pastes unify many of the design requirements^[16] mentioned earlier. The addition of gelatin as a viscosity modifier provides additional processability, applicability, and even architectural benefits because the solder can be formulated as a non-sticky, stable (layered) gel, easily shaped, and cut by surgeons before application (Figure 1e). Complex shapes can be readily cut using regular surgical scissors and can be handled and positioned on tissue with tweezers. As gelatin liquefies at elevated temperatures during soldering, the solder forms an optimal interface with the biological tissue regardless of its topology.

iSoldering is achieved by adding nanoparticulate enhancers (thermoplasmonics and nanothermometers) to the protein-based solder base material. Nano-absorbers operating in the biological transparency window are exploited to convert light into heat via thermoplasmonic processes, enabling confined heating at the solder–tissue interface. Specifically, gold nanorods (GNRs) can be tuned to selectively absorb any wavelength in the biological windows (650–950 nm and 1000–1350 nm). Alternatively, broadband-absorbing and more affordable titanium nitride (TiN) nanoparticles (Figure 1c) may be integrated into the solder material.

Additionally, nanothermometers in the form of flame-synthesized $\text{BiVO}_4:\text{Nd}^{3+}$ (Figure 1c; Supporting Information S1 for characterization data) are incorporated into the solder base, offering direct, non-invasive, real-time temperature monitoring capabilities via fluorescence near-infrared nanothermome-

try. Specifically, the composition of the nanoparticle-enhanced solder is selected to either have coupled excitation of the heating material and the fluorescent nanothermometers (as is the case for TiN and $\text{BiVO}_4:\text{Nd}^{3+}$) or decoupled excitation (GNRs and $\text{BiVO}_4:\text{Nd}^{3+}$). While only one laser is required in the first case, some of the emitted light from the nanothermometers is also absorbed by the TiN because of its broadband and constant absorbance (Figure 1f).

By contrast, GNRs and $\text{BiVO}_4:\text{Nd}^{3+}$ have minimal spectral overlap and permit decoupling of the heating and monitoring. This is possible because of the deliberate choice of longer GNRs, with an aspect ratio above 6.5, low absorbance at excitation and emission wavelengths, and an absorption peak in the second biological window where laser light is expected to penetrate the tissue more deeply. Nanomaterial-augmented iSoldering is designed to transform conventional laser tissue soldering (Figure 1g) into safe, high-performance soldering based on the controlled cross-linking of tissue interface proteins and the absence of tissue damage due to temperature monitoring by non-invasive fluorescence nanothermometry (Figure 1h).

2.2. Simulation-Based iSolder Optimization

Because of ample design space and synthetic capabilities, the solder design (composition, and especially architecture) was further optimized by developing a computational model (Figure 2a). The finite element analysis (FEA) heat diffusion simulations permit clear visualization of the operating benefits in the biological tissue windows and the use of NIR lasers or medically approved water-filtered near-infrared light (wIRA) compared to green or UV laser light (Figure 2b).

The biological tissue is heated by green and blue laser light to temperatures of 60 °C even in the absence of nanoabsorbers in conditions feasible for soldering, reaching dangerously high temperatures in a matter of seconds. However, no relevant temperature increase can be observed for the NIR lasers at equivalent power densities (Figure 2b).

Additionally, the temperature distribution during laser irradiation of a solder paste placed on a biological tissue was studied with different solder paste formulations. The FEA indicated strong concentration dependence and the clear benefits of adding nanoheaters (both TiN and GNRs, Figure 2c,d, respectively). Photothermal agents absorb light very efficiently, permitting better localization and confinement of solder–tissue interface heat production and diminishing the off-target energy deposition in the underlying tissue. This enables the choice of a laser with a power and irradiance that is safe for healthy biological tissues.

Importantly, these simulations also suggest conditions where heating is inefficient in the absence of these nanoheaters (i.e., in nanoabsorber-devoid tissue) and temperature only marginally increases in the timeframes relevant for soldering (4 min of laser irradiation, vide infra) at the same laser power. In other words, these results strongly indicate that relevant temperature increases are only reached in areas containing nanoheaters and not in the surrounding tissue for optimized laser settings with well-positioned nanoheaters. A concentration of nanoheaters at the tissue interface (and not in the solder's top layers) enables maximal interface temperature increase where the bond is

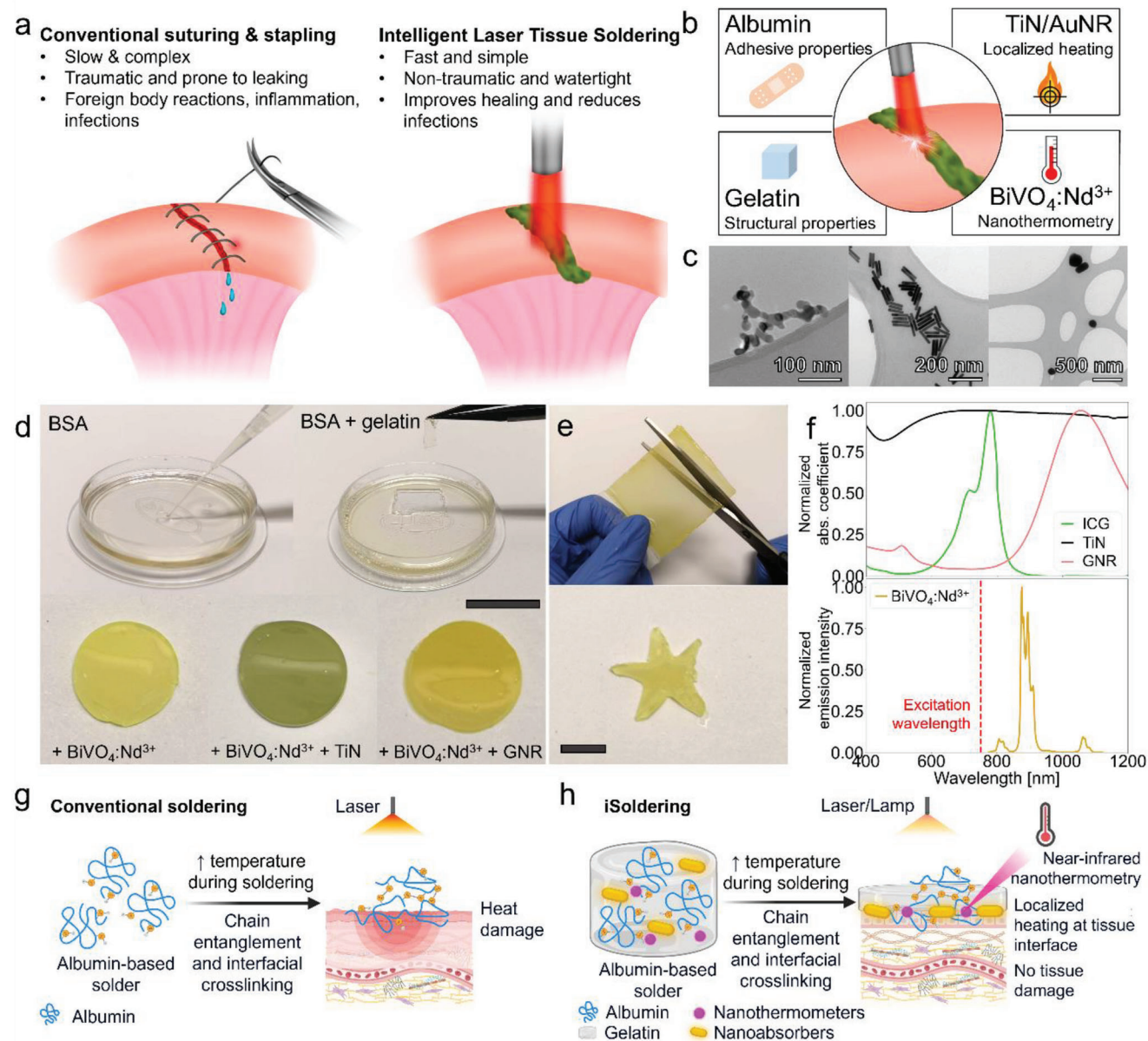


Figure 1. Design and mechanism of iSolder. a) Intelligent Laser Tissue Soldering (iSoldering) vs. conventional suturing or stapling. b) Illustration of the various solder paste components and their function. c) Transmission electron micrographs of the nanoparticle enhancers, from left to right: TiN, GNRs, and BiVO₄:Nd³⁺. d) Photographs of various solder paste compositions. The bovine serum albumin (BSA) paste is initially liquid and exhibits a gel-like behavior upon adding gelatin (6.5 wt.%). In the bottom row, BSA + gelatin solders with the addition of the different nanoparticle enhancers are shown. e) The addition of gelatin enables easier handling and shaping of the article. Complex shapes can be readily cut using standard surgical tweezers (black scale bar = 0.5 cm). f) Absorption spectra of the light-absorbing candidate materials indocyanine green (ICG), TiN, and GNRs, and the fluorescence spectrum of BiVO₄:Nd³⁺ nanothermometers. g) Illustration of conventional soldering and h) iSoldering enabling localized heating and deep tissue thermometry, facilitating safe, high-performance soldering.

formed and avoids blocking the light and cross-linking of the solder surface. Importantly, the simulation also shows that the solder surface temperature is not representative of the temperature of the solder–tissue interface (Figure 2e). Although the solder–tissue interface temperature is of the utmost importance in the soldering process because it determines the adhesion properties, this information is not readily retrieved by available techniques such as thermal cameras. These findings likely also explain some

of the heat damage and reproducibility issues for laser tissue soldering reported in the literature.^[45]

2.3. Optimization of the iSolder Composition

Our goal was to achieve optimal and robust performance in a safe-by-design manner. Therefore, we experimentally optimized

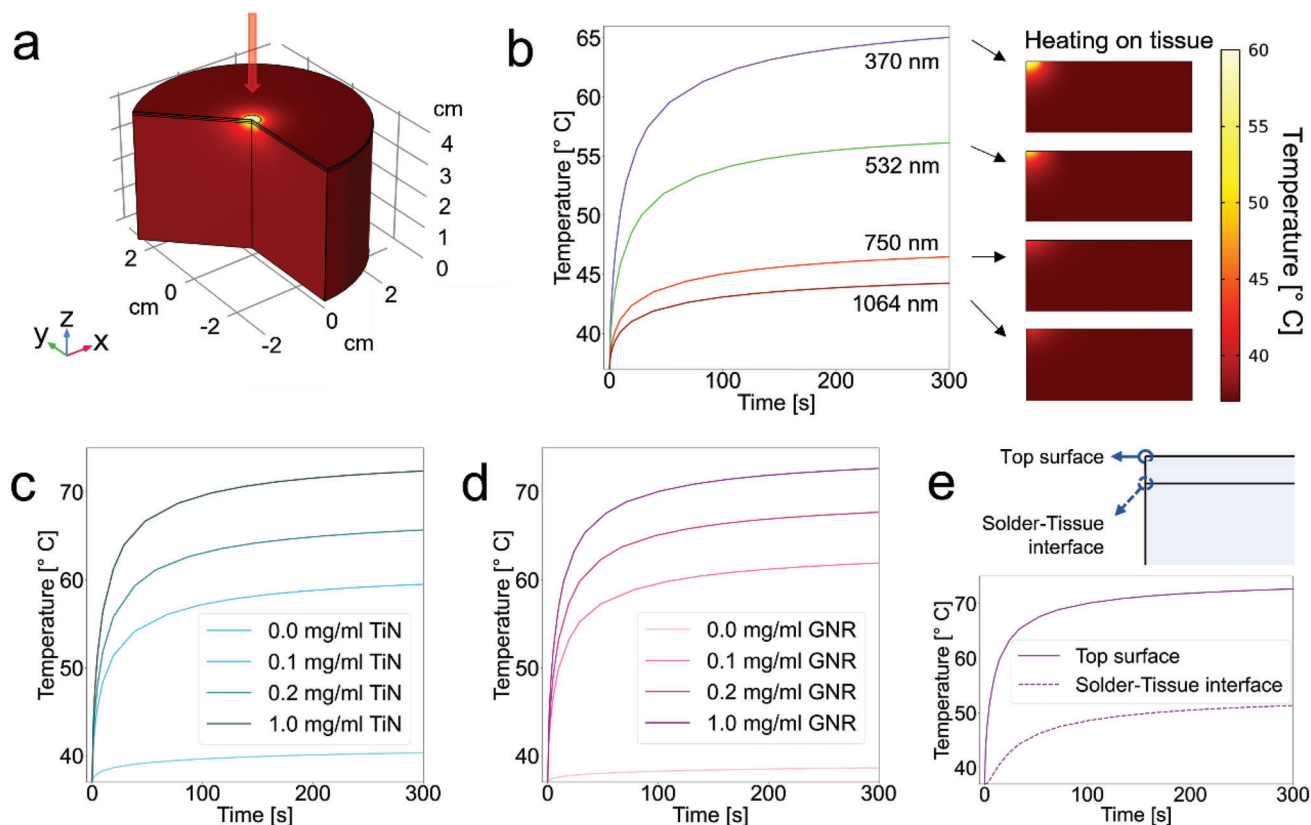


Figure 2. Simulation-based iSolder optimization. Finite element analysis (FEA) of temperatures reached during laser irradiation with different wavelengths and solder compositions. a) 3D model geometry used in the simulation. b) Temperatures reached during laser irradiation on tissue using different wavelengths. The time dependence of the maximum temperature is shown on the left side, while the tissue temperature distribution is shown on the right side. c) Temperatures reached during soldering using a 750 nm laser and a TiN-based solder paste. d) Temperatures reached during soldering using a 750 nm laser and a GNR-based solder paste. e) Temperatures at the top solder surface and solder–tissue interface can differ substantially during soldering. A laser with 0.1 W power and a 0.5 cm beam diameter was used for the simulations.

the solder composition to reach a suitable temperature increase at a feasible and biologically acceptable laser power and an acceptable nanothermometry readout signal-to-noise ratio. As expected, the temperature increase increases as more nanoabsorbers are added, which is also consistent with the simulations (Figure 2c,d). However, the experimental study provides more comprehensive information because it accounts for additional effects, including phase changes. The emission of the BiVO nanoparticles shows a strong dependence on the local temperature with a sensitivity of 1.47%/K in the relevant laser tissue soldering range.^[46] Note that the nanothermometer response is very robust and largely independent of the solder composition and environment (Figure 3a,b), making lanthanide-based nanothermometry a particularly appealing choice for the intended application.

Regarding the nanothermometry signal, it is evident that a higher BiVO concentration corresponds to higher fluorescence counts (Figure 3c,d). However, in the case of the TiN, the fluorescence counts of the BiVO strongly decrease with increasing TiN concentration, as expected because of TiN's broadband absorbance. This effect is much less pronounced for gold because of its much sharper absorption peak and its correspondingly lower overlap with the BiVO emission (Figure 1e). Interestingly,

however, for combinations of nanoabsorbers with BiVO, it is also evident that the addition of BiVO nanoparticles leads to a synergistic heating effect exceeding the sum of the individual particle effects (Figure 3e–h). This effect, which was consistently observed in the tests at various concentrations, could be due to various factors, such as higher scattering due to BiVO nanoparticles that lead to more scattered photons that can therefore be absorbed by nanoheaters, fluorescence reabsorption, and other interactions between particles. Based on the latter compositional optimizations, we concluded that for our laser-spectrometer configuration, the particle concentrations of 0.025–0.1 mg mL⁻¹ (i.e., 0.0025–0.01%) for nanoheaters and 2–3 mg mL⁻¹ (i.e., 0.2–0.3%) for nanothermometers are an optimal compromise between performance (heating within 1 minute up to the target temperature of 60 °C and signal-to-noise ratio higher than 30:1 with 1 s integration time), nanoparticle dose (cf. toxicity), and cost.

2.4. iSolder Performance and Deep Tissue Soldering

The performance of these new solder paste formulations was thoroughly investigated in two different configurations: soldering of i) a superficial wound and ii) a deep tissue wound. These

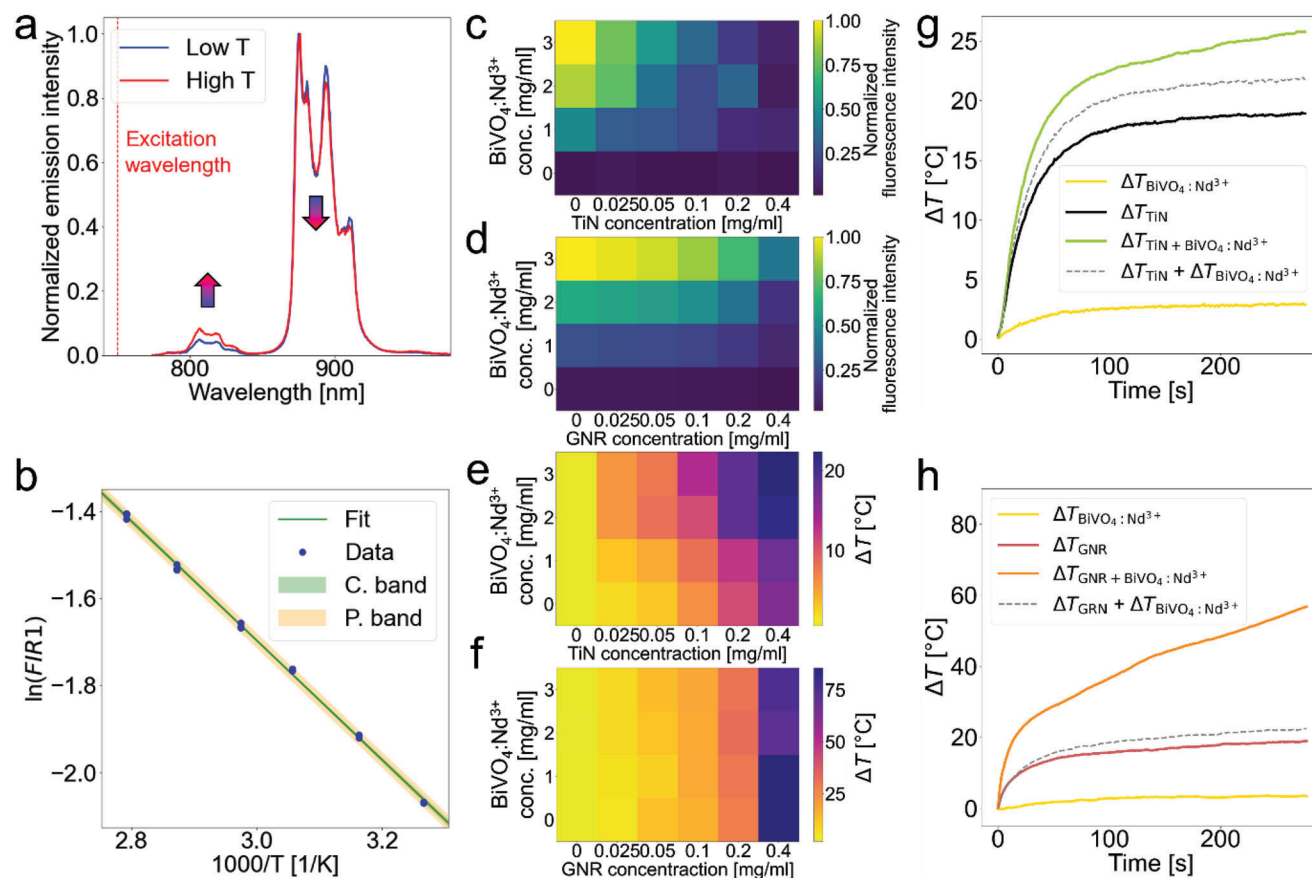


Figure 3. Integration of temperature-monitoring modalities into iSolder and optimization of concentration and composition. a) Emission spectra of the nanothermometers at low and high temperatures (35 and 71 °C respectively) show two distinct peaks that change in intensity based on the temperature, as indicated by the arrows. b) Calibration curve used for temperature measurements, relating the ratio between the two peaks (FIR) and the temperature T . The fit is presented with confidence and prediction bands. c–f) Nanoconcentration optimizations for c,e) BiVO + TiN and d,f) BiVO + GNR showing c,d) fluorescence intensity and e,f) temperature increase (ΔT) after 30 s at different nanoenhancer concentrations. 750 nm laser: power = 1.25 W, spot size diameter = 0.8×0.9 cm. 1064 nm laser: power = 1.29 W, spot size diameter = 0.4×0.3 cm. g–h) Illustrative examples of the temperature increases observed during soldering for two different solder paste compositions. Higher temperatures are achieved using a paste containing both types of nanoenhancers instead of either type alone (top: BiVO 0.2% + TiN 0.003% – 750 nm laser with 0.886 W in 1.18 cm²; bottom: BiVO 0.3% + GNR 0.01% – 1064 nm laser with 1.29 W in 0.094 cm²). Measurements were carried out in triplicates ($N = 3$).

were benchmarked against state-of-the-art temperature measurements by a thermal camera. Soldering performance was assessed after validating the nanothermometry method, compared with reference temperatures measured by the thermal camera in a temperature-controlled setting (Figure 4a). Comparison of the reference thermometer and the nanothermometers (in the surface and deep tissue configurations, Figure 4b) showed excellent agreement (Figure 4a) for the different measurement modalities, indicating functionality and proper calibration of the two experimental methods used for the remaining experiments.

Because of the GNRs' wavelength-dependent absorption, decoupling of heating and sensing can be achieved using a two-laser system with the BiVO/GNR solder paste (Figure 4c). The 750 nm laser can be used to measure the temperature without significantly heating the paste. The 1064 nm laser increases the temperature, and its power can be modulated without affecting the temperature measurement. These measurements also confirm the feasible temporal resolution of nanothermometry compared with the thermal camera-based temperature measure-

ments. Both iSolder formulations can reach the necessary target temperatures in both the surface and the deep tissue configurations (Figure 4d). While the temperatures measured by the thermal camera and the nanothermometry are in good agreement in the surface configuration, the thermal camera dangerously underestimates the temperatures reached during soldering in the deep tissue configuration.

Importantly, these measurements indicate the promising potential of iSoldering beyond superficial wounds, such as deep tissue wounds and defects. Note that the iSolder design ensures heating only in the nanoabsorber-containing regions (i.e., the solder) and nanothermometry accurately measures the temperature of the most relevant area exclusively, namely the solder paste containing the light-absorbing particles, for both paste formulations.

Moreover, the fluorescent nanothermometry signal can be readily used to provide feedback to the heating process. A simple PID controller (i.e. proportional-integral-derivative controller, a widely used control loop mechanism using three control terms) based on the nanothermometry signal is used to automatically

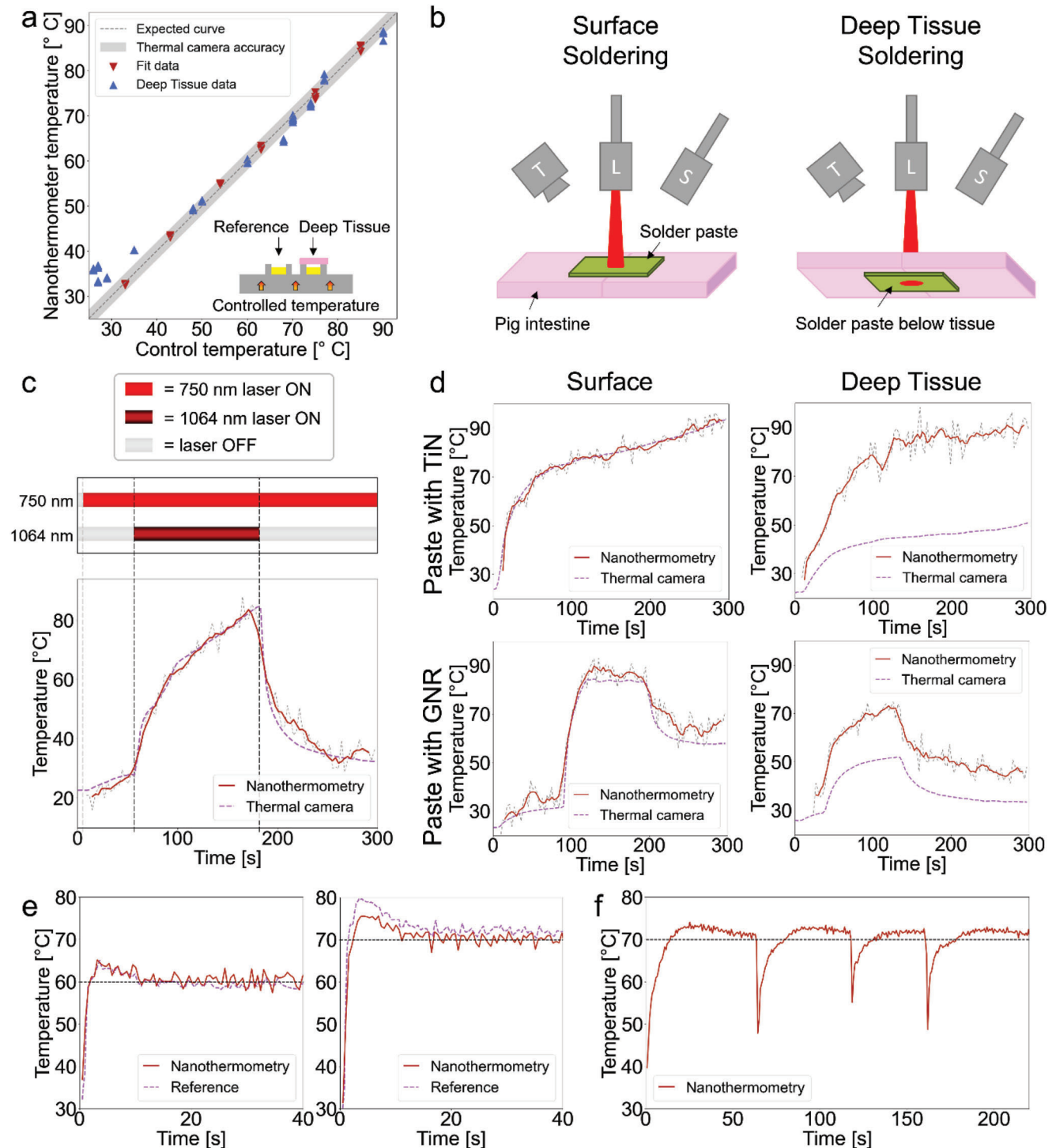


Figure 4. Nanothermometry enables deep tissue soldering. Superficial and deep tissue soldering with temperature monitoring using a thermal camera and nanothermometers, respectively. a) Agreement between control temperature and nanothermometry-measured temperatures. b) Schematic of the two soldering configurations used in this work. c) Temperature evolution during soldering measured by nanothermometry and reference thermometers shows good agreement and reasonable temporal resolution. Decoupling the temperature and heat measurements is possible using a dual-laser configuration. d) Temperature measurements during soldering with the different pastes (BiVO/TiN and BiVO/GNR) in both configurations (superficial and deep tissue). Note that thermal cameras underestimate the temperature in the deep tissue configuration, while the nanothermometry-based measurements give access to the effective temperature. e) A feedback-controlled loop based on the nanothermometry signal can be used to modulate the laser power to achieve a pre-set target temperature, here 60 or 70 °C, which is also validated by the reference measurements. f) Controlled temperature can also be achieved while moving along the wound. Measurements were carried out in triplicates ($N = 3$).

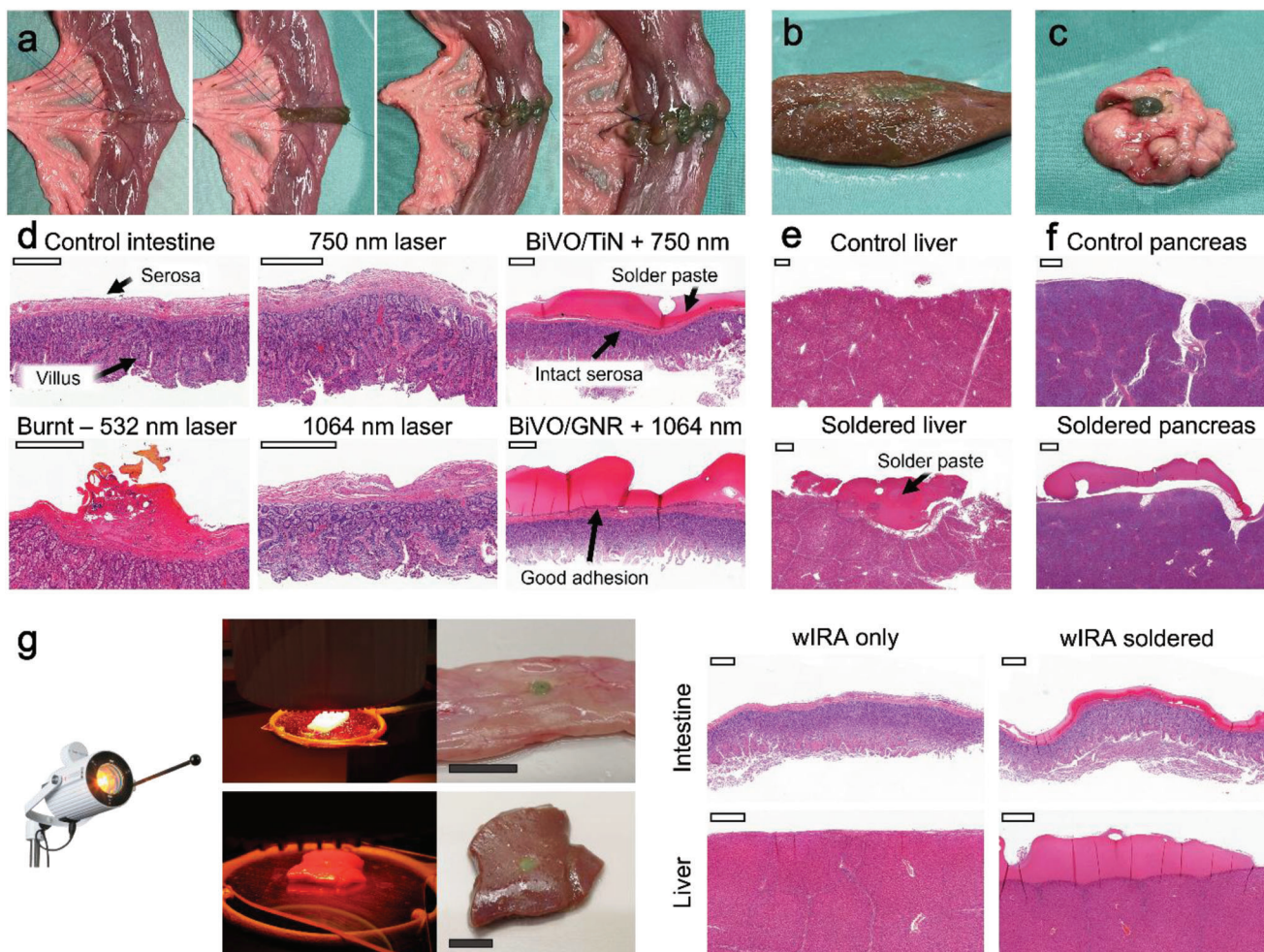


Figure 5. Ex vivo iSoldering of intestinal anastomoses, non-anatomic liver resection surfaces, and pancreas defects. Straightforward application of iSoldering to a sutured a) intestinal anastomosis, b) liver, and c) pancreas. d) Histological analysis (H&E staining) shows intact intestinal tissue for all soldered samples (4 min illumination with 750 nm laser, 2.58 W cm^{-2} , or 1064 nm laser, $8.11 \text{ W } 0.5\text{cm}^{-2}$) and no visible thermal damage, as opposed to intestinal tissue exposed to green laser light (wavelength 532 nm, power density 7.5 W cm^{-2}). Histological analysis of untreated and soldered e) liver and f) pancreas tissue. g) Medically-approved, water-filtered infrared light (wIRA) irradiation employed for iSoldering of intestine and liver samples and corresponding histological analysis (H&E) of soldered intestine and liver tissue samples. White scale bars = 0.5 mm. Black scale bars = 1.5 cm. Representative micrographs shown from $N = 3$ independent applications.

modulate the laser power to achieve and maintain the target soldering temperature (Figure 4e). This automatic temperature control provides a robust mechanism and can also be operated when soldering is performed moving along the soldering region (Figure 4f).

2.5. Versatile and Safe Tissue Sealing

Next, we sought to demonstrate that iSoldering enables rapid and robust leak-tight tissue sealing of diverse tissues and geometries, including end-to-end intestinal anastomoses (Figure 5a), non-anatomical liver resections (Figure 5b), and pancreatic tissue sealing (Figure 5c). Macroscopic analysis shows strong tissue adhesion. Histological analysis of the soldered tissues confirms tight contact between the solder and the tissue surfaces (Figure 5d–f), especially compared with alternative tissue adhe-

sives and sealants^[3]. Soldered tissue appears indistinct from untreated control or tissue exposed to NIR laser irradiation only (for 4 min, equivalent to the soldering time). No damage can be seen macroscopically or histologically due to heating in contrast to tissue burned using a green laser at similar power intensities and illumination times (Figure 5d).

Interestingly, instead of a NIR laser, medically-approved water-filtered infrared (wIRA) light can also be employed for soldering to overcome operating room laser safety barriers. wIRA light consists of infrared-A radiation with a strong decrease in emission in the wavelengths absorbed by water and it is therefore weakly absorbed by most tissues. The soldering using non-damaging, safe-for-use wIRA light shows equivalent tissue adhesion with no indication of tissue damage (Figure 5g). Soldering with wIRA is only possible because the TiN nanoparticles in the solder paste permit its broadband absorption spectrum to absorb most of the light emitted by the wIRA lamp, in contrast

with dyes or plasmonic particles with narrower absorption regions.

2.6. In Vivo Proof-of-Concept in a Porcine Model

Finally, we sought to demonstrate the iSolder approach's versatility by application to diverse tissues and organs in an operating theatre environment using a porcine model. iSoldering was applied to create a leak-tight seal in an end-to-end anastomosis of a small intestine (Figure 6a), the ureter (Figure 6b), a fallopian tube (Figure 6c), and the renal vein (Figure 6d) of a piglet. The absence of visible damage and good adhesion to the tissue was also maintained after the soldered tissue was returned to the abdominal cavity in contact with other tissues (Figure 6a). iSoldering again showed excellent tissue contact and penetration into the defect and straightforward application by the operating room surgeons in all these applications with minimal preparation or training required. Additionally, solder stability in the presence of simulated intestinal fluid (Figure 6e) was quantified, revealing that the soldered materials resisted digestion for exposure periods of at least 7 days, in contrast to non-soldered precursors that disintegrated within minutes when exposed to phosphate-buffered saline or intestinal fluids.

In addition to the above macroscopic and histological investigations, we assessed tissue sealing based on impermeability to bacteria and dye-leaking experiments using methylene blue. No bacteria leakage was observed in the soldered tissue compared with defective tissue where bacteria leakage occurred within minutes (Figure 6f). Moreover, the dye-leaking test showed no leaking in solder-reinforced sutures compared with sutured samples at similar pressures (Figure 6g). Burst pressure measurements further demonstrate this technique's potential to increase watertightness. When applied to a sutured wound on the small intestine, iSoldering improves the burst pressure by more than 70% relative to sutures alone. This can be explained by the sealing action on suture defects by the solder paste. Strong adhesion is further confirmed by the tensile strength values reached for soldered tissues compared with intact tissues in both surface and deep tissue configurations (Figure 6h).

3. Conclusion

This work has introduced the iSoldering concept to overcome the significant shortcomings of laser tissue soldering. iSoldering is based on two innovative steps: the integration of nanothermometers and the confinement of the heat-absorbing layer to the surface (melting gel). iSoldering facilitates safe, high-performance, leak-tight tissue fusion using a minimally-invasive technique, enabling enhanced sealing and reduced infection risk compared with contemporary suturing or stapling. Importantly, this work exploits (fluorescence) nanothermometry for laser tissue soldering for the first time. This technique permits prospective new applications, including possible safe and precise deep tissue soldering and risk-free soldering in endoscopic/laparoscopic settings or even robotic surgery. iSoldering may become particularly powerful in laparoscopic and robotic surgeries where current issues related to incorrect suture positioning or tightening cause scar tissue due to epidermal ingrowth along the suture track, as well as

premature loss of tensile strength.^[10,46] This "intelligent" soldering concept may enable high-performance soldering and offer a platform for further fundamental mechanistic investigations, enabling data-driven optimization of soldering technology for specific clinical needs in the fields of cardiovascular, visceral, plastic, orthopedic, or neurosurgery.

4. Experimental Section

Nanothermometer Synthesis: BiVO₄:Nd³⁺ (or BiVO) was produced using liquid-fed flame spray pyrolysis based on methods described previously.^[46] Briefly, Bi(NO₃)₃ · 5H₂O (bismuth nitrate pentahydrate – Sigma-Aldrich, 248592) and Nd(NO₃)₃ · 6H₂O (neodymium nitrate hexahydrate – Sigma-Aldrich, 289175) were dissolved separately in a 2:1 volumetric mixture of 2-ethylhexanoic acid (Sigma-Aldrich, E29141) and acetic anhydride (Sigma-Aldrich, 8.22278.1000). They were mixed by magnetic stirring at room temperature until complete dissolution, reached after ≈2 h.

NH₄VO₃ (ammonium metavanadate – Fluka, 10030) was dissolved separately in a 2:1 volumetric mixture of 2-ethylhexanoic acid and acetic anhydride. These were magnetically stirred at 100 °C until complete dissolution, achieved after ≈2 h.

The two solutions were then mixed to form the precursor solution. The Nd³⁺ concentration was defined as the atomic fraction (at.%) of the total metal ion concentration resulting in Bi_{0.99}Nd_{0.01}VO_{0.4}, chosen based on its high luminescence intensity. The total metal concentration was maintained at 0.4 M.

The precursor solution was fed at a constant 8 mL min⁻¹ rate through a nozzle and dispersed by 3 L min⁻¹ of oxygen. The resulting fine spray was ignited and sustained by a surrounding premixed oxygen/methane (1.5/3.2 L min⁻¹) flamelet. The particles were collected on a glass microfiber filter (Whatman GF) with a vacuum pump (Busch Mink MM 1202 AV). The particles were scraped out of the filter and sieved (sieve aperture of 0.250 mm). Annealing of the particles was carried out at 600 °C for 6 h (Carbolite Gero LHT6/30).

Nanoparticle Characterization: Transmission electron microscopy (TEM) of BiVO, TiN, and GNR nanoparticles was carried out using an EM900 transmission electron microscope from Carl Zeiss Microscopy GmbH at 80 kV. For grid preparation of the BiVO and TiN samples, holey carbon-coated copper grids (200 mesh, EM Resolutions) were incubated with poly-L-lysine solution (P8920, Sigma-Aldrich) for 10 min and subsequently washed with ultrapure (milliQ) water. The BiVO, TiN, and GNR samples were dispersed in milliQ water and then drop-casted onto the poly-L-lysine-treated holey carbon-coated copper grids for BiVO and TiN, or onto graphene oxide holey carbon-coated copper grids for the GNRs (300 mesh, EM resolutions). Absorption spectra were measured using a UV-vis-NIR spectrophotometer (Cary 500 Scan), and fluorescence was measured using a NIR spectrometer (OceanOptics STS-NIR, 100 μm slit). Additional BiVO characterization is provided in Supporting Information S1.

Solder Paste Preparation and Characterization: The solder paste preparation started with concentrated solutions of bovine serum albumin (BSA, Sigma-Aldrich, A2153), gelatin (from porcine skin, gel strength 300, Type A – Sigma-Aldrich, G2500), and various nanoparticles. BSA was dissolved in deionized water and left to hydrate on a shaker overnight at room temperature. Gelatin was dissolved in deionized water and heated in a shaker at 60 °C for several hours. Flame-made BiVO₄:Nd³⁺ and TiN nanoparticles (PlasmaChem GmbH, PL-HK-TiN) were separately dispersed in distilled water and sonicated (Bradson 1800) for at least 15 min. GNRs with aspect ratios of 6.7 and diameters of 10 nm (Nanopartz, A12-10-1064-CIT-DIH-1-25) were concentrated using centrifugation for 15 min at 10 rcf (VWR MicroStar12).

The solder paste was created by mixing the appropriate amounts of concentrated stock solutions and diluted with distilled water when necessary. The solutions were mixed quickly using a vortex, ensuring that the gelatin could not solidify before casting the solution into the appropriate mold

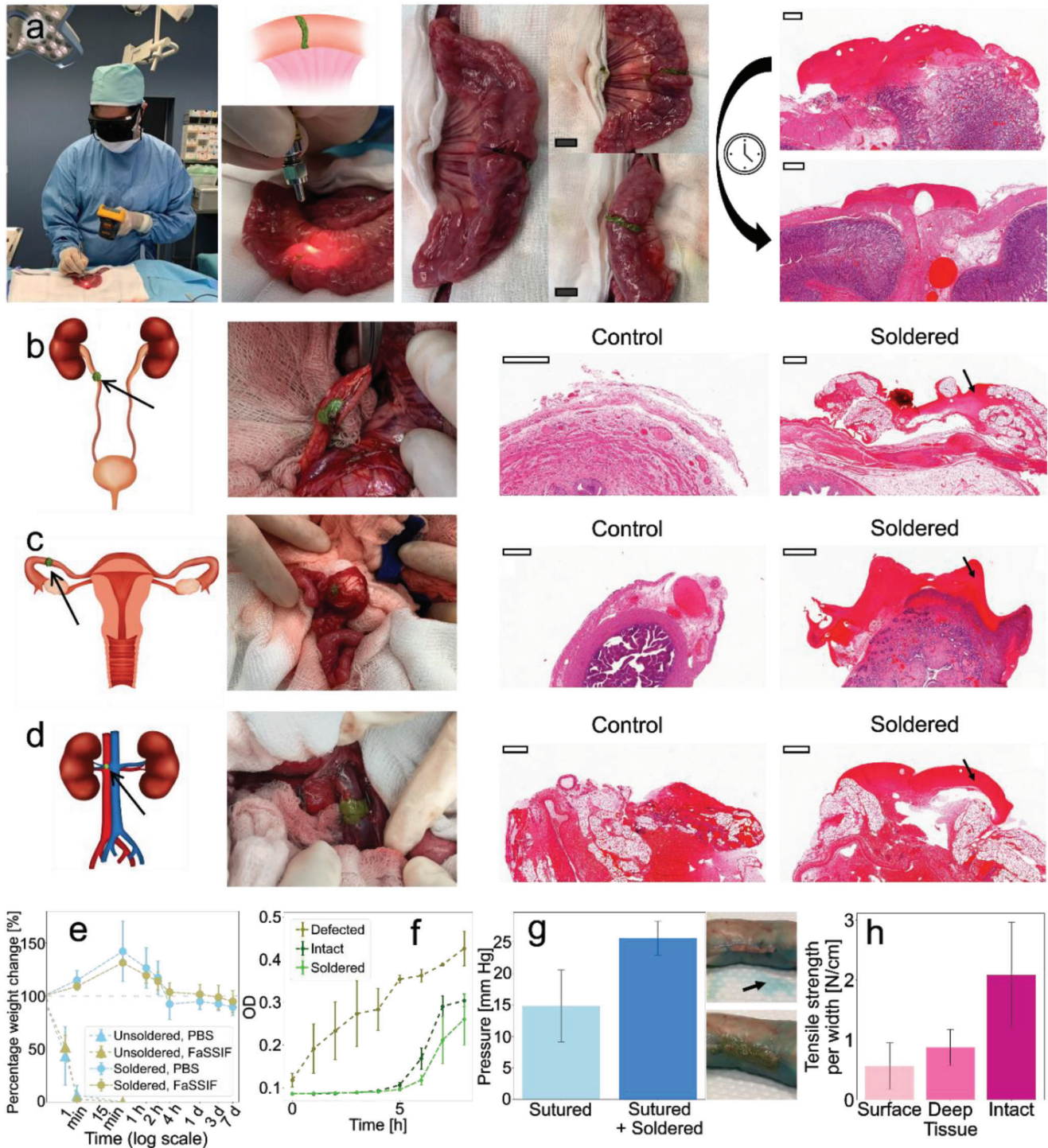


Figure 6. In vivo application of iSoldering to diverse tissues in a porcine model. a) Straightforward application of iSoldering to a sutured intestinal anastomosis (black scale bar = 1.5 cm). After two hours in the abdominal cavity, H&E staining shows strong adhesion, no tissue damage, and leak-tight sealing (as illustrated by inflation of the intestine). Application of iSoldering to an anastomosis at the level of the b) ureter, c) fallopian tube anastomosis, and d) renal vein defect. White scale bars = 0.5 mm. e) The iSolder seal was highly stable even in the presence of digestive fluids, i.e., FaSSIF (fasted state simulated intestinal fluid) for at least 7 days at 37 °C, in contrast to the unsoldered starting material. f) The soldered intestine can avoid bacterial leakage, as seen by the absence of extraluminal bacteria. g) iSoldering leads to increased burst pressure compared to a sutured intestine. A leak-tight seal is achieved as illustrated by perfusion with methylene blue (the top image shows a sutured-only intestine with fluid leaking indicated by the arrow; the bottom image shows the soldered intestine without leaking). h) Tissue adhesion in tensile tests for superficial and deep tissue soldering configurations compared to native (intact) tissue. N = 3 independent experiments for (e–h).

Table 1. Parameters used in the simulations.

Symbol	Parameter name	Solder (without nanoparticles)	Tissue
ρ	Density [kg m ⁻³]	895 ^[48]	1030 ^[49]
C_p	Specific heat capacity [J kg ⁻¹ K ⁻¹]	3353.5 + 5.2 · T ^[48]	3595 ^[50]
k	Thermal conductivity [W m ⁻¹ K ⁻¹]	0.3528 + 0.0016 · T ^[48]	0.49 ^[50]
$\mu_{\text{abs}}(\lambda)$	Absorption coefficient [cm ⁻¹]	0.158	6.456 ($\lambda = 370$ nm) 2.054 ($\lambda = 532$ nm) 0.07540 ($\lambda = 750$ nm) 0.07924 ($\lambda = 1064$ nm)
$\mu'_{\text{scat}}(\lambda)$	Reduced scattering coefficient [cm ⁻¹]	0.01	2.399 ($\lambda = 370$ nm) 1.529 ($\lambda = 532$ nm) 0.9990 ($\lambda = 750$ nm) 0.6475 ($\lambda = 1064$ nm)
B	Blood volume fraction	–	0.0093
S	Oxygen saturation of hemoglobin	–	0.8
W	Water volume fraction	–	0.5
a	Scattering parameter a	–	3670
b	Scattering parameter b	–	1.27
ϵ	Surface emissivity	0.95	0.95

(e.g., a hard plastic well or a flexible plastic sheet). The paste was formed by cooling the solution at 4 °C for at least one hour and then stored at that temperature in an airtight container. All pastes were used within the first 2 weeks after production.

Simulation: COMSOL Multiphysics 6.0 was used to create a finite element model of the soldering process to qualitatively investigate the effects of laser heating on intestinal tissues and solder paste.^[20] The system was modeled as a two-layered system with cylindrical symmetry. The solder paste (with subscript S) and the tissue (with subscript T) were modeled as a homogeneous layer with heights $h_S = 0.2$ cm, $h_T = 4$ cm and radii $r_S = 3.25$ cm, $r_T = 3.25$ cm. A continuous wave (CW) laser beam with variable wavelength λ , power I and radius r_L impinged from the top onto the system's center. The initial temperature of the system was set at 37 °C. The time-dependent spatial temperature distributions in the solder pastes and tissue were modeled using the heat transfer equation

$$\rho C_p \frac{\partial T}{\partial t} + \nabla \cdot (-k \nabla T) = Q_{\text{ext}} \quad (1)$$

where ρ is the density, C_p is the specific heat capacity, T is temperature, t is time, k is the thermal conductivity, and Q_{ext} represents the heat received from external sources, such as from laser energy absorption (Q_{laser}), air convection (Q_{conv}) or radiation heat loss (Q_{rad}). Therefore, $Q_{\text{ext}} = Q_{\text{laser}} + Q_{\text{conv}} + Q_{\text{rad}}$. The heat absorbed from the laser beam was modeled using the Beer–Lambert law, expressed in cylindrical coordinates as

$$Q_{\text{laser}} = - \frac{\partial I(r, z)}{\partial z} = \mu_{\text{abs}} I(r, z), \quad (2)$$

$$I(r, z) = I_0(r) e^{-(\mu_{\text{abs}}(\lambda) + \mu'_{\text{scat}}(\lambda))z}, \quad (3)$$

where $I_0(r)$ is the laser intensity at the upper surface, $\mu_{\text{abs}}(\lambda)$ is the absorption coefficient at wavelength λ , and $\mu'_{\text{scat}}(\lambda)$ is the reduced scattering coefficient at wavelength λ . The reduced scattering coefficient μ'_{scat} is often used in the biomedical optics community instead of the scattering coefficient μ_{scat} since it considers the medium anisotropy g and is defined as $\mu'_{\text{scat}} = \mu_{\text{scat}}(1 - g)$. The absorption coefficient for the intestinal tissue was calculated as the sum of the absorption contributions from water and hemoglobin^[48] using the formula

$$\mu_{\text{abs},T}(\lambda) = B \left(S \times \mu_{\text{abs,oxyHb}}(\lambda) + (1 - S) \times \mu_{\text{abs,deoxyHb}}(\lambda) \right) + W \mu_{\text{abs,water}}(\lambda) \quad (4)$$

where B is the blood volume fraction, S is the oxygen saturation of hemoglobin in the tissue, W is the water volume fraction and $\mu_{\text{abs,oxyHb}}(\lambda)$, $\mu_{\text{abs,deoxyHb}}(\lambda)$, and $\mu_{\text{abs,water}}(\lambda)$ are the absorption coefficients of oxygenated hemoglobin, deoxygenated hemoglobin, and water, respectively. The scattering coefficient for the intestinal tissue was calculated using the equation $\mu'_{\text{scat},S}(\lambda) = a \times \lambda^{-b}$ mm⁻¹ (with λ in nm), where a and b are constants specific to the tissue of interest. The absorption and scattering coefficients of the solder paste were changed based on the number of nanoparticles added to it based on UV–vis measurements.

The convection heat loss Q_{conv} was modeled as $Q_{\text{conv}} = -h(T - T_{\text{atm}})$ where h is the convection heat transfer coefficient and T_{atm} is the air temperature, equal to 37 °C. The radiation heat loss was modeled using the equation $Q_{\text{rad}} = -\epsilon \sigma (T^4 - T_{\text{atm}}^4)$ where ϵ is the surface emissivity and σ is the Stefan–Boltzmann constant.

An appropriate discretization was chosen by examining the stability of the results. The final mesh was created using triangles, imposing 60 and 30 elements along the axes in the solder paste and tissue regions, respectively. The minimum and maximum element sizes were set to 9.75×10^{-6} m and 1.72×10^{-3} m respectively, with a maximum element growth of 1.3, curvature factor of 0.3, and resolution of narrow regions of 1.

The list of the values of parameters used in the simulation is presented in **Table 1**.

Optimization of Solder Paste: Solder pastes made of 25% BSA, and the various particle concentrations were created and placed in 3D-printed transparent resin cylindrical wells (1 mm high, 10 mm diameter). Triplicates were used for each concentration. Fluorescence was acquired for 30 s with a 10 s integration time. A thermal camera (Optris PI 640i with microscope optics) measured the temperature during irradiation. The temperature after 30 s was used to create the concentration plots in **Figure 3**.

Soldering of Ex Vivo Samples and Thermal Sensing: Porcine small intestine, liver, and pancreas were collected from a slaughterhouse on the same morning of the experiment. Samples were cut into pieces of the desired shape using a surgical scissor or a scalpel. Pieces of the intestine were maintained at a low temperature and hydrated by spraying with PBS when necessary.

The solder paste was placed on the intestine piece and irradiated by one or two lasers. Two different lasers were used, a 750 nm continuous wave (CW) laser (MDL-III-750, CNI Laser) with a 1.9 W maximum power output and a 1064 nm CW laser (Ventus 1064, Laser Quantum Ltd) with a 1.5 W maximum output. A power meter (Gentec-EO SOLO PE) measured the laser powers.

A CMOS camera and a viewing card measured the laser spot size. Band-pass filters with corresponding wavelengths filtered out unwanted wavelengths produced by the laser (750 nm: FB750-40, Thorlabs; 1064 nm: FLH1064-10, Thorlabs). A compact spectrometer (STS-NIR, OceanOptics) measured the fluorescence spectra of the nanoparticles. Two 785 nm long-pass filters (47-508, Edmund Optics) and a 1000 nm short-pass filter (FES1000, Thorlabs) were employed to filter the laser light. A collimator (FOC-01, CNI Laser) was applied to increase fluorescence collection. The fluorescence signal was fed to the spectrometer through a multimode fiber (NA = 0.22, core diameter = 0.600 mm). The spectrometer was placed ≈5 cm away from the solder paste. Background and offset corrections were performed during data analysis, using the wavelengths between 632.985 nm and 656.351 nm as references, which are far from excitation and emission peaks.

The Boltzmann thermal equilibrium equation links the emission spectrum with temperature:

$$FIR = C_1 \exp\left(-\frac{\Delta E}{k_B T}\right) \rightarrow \ln(FIR) = C_2 - \left(\frac{\Delta E}{k_B}\right) \frac{1}{T} \quad (5)$$

where *FIR* is the fluorescence intensity ratio, defined as $FIR = I_1 / I_2$, with I_1 the fluorescence intensity given by the ${}^4F_{5/2} \rightarrow {}^4I_{9/2}$ transition (≈820 nm) and I_2 the fluorescence intensity ${}^4F_{3/2} \rightarrow {}^4I_{9/2}$ transition (≈870 nm). ΔE is the energy difference between the two emissions (${}^4F_{5/2} \rightarrow {}^4I_{9/2}$ and ${}^4F_{3/2} \rightarrow {}^4I_{9/2}$), k_B is the Boltzmann constant, T is temperature, and C_1 and C_2 are fitting constants that depend on the material. This relation linearly relates the logarithm of the fluorescence intensity ratio with the inverse of the temperature: $y = a + b \times x$ with $y = \ln(FIR)$ and $x = 1/T$. The intensities I_1 and I_2 can be computed after defining the intervals around the peaks to be used for the temperature measurement.

While a broader interval leads to more precise measurements, this could lead to less accurate results for low fluorescence counts because bias errors from the electronics are more relevant in parts with low counts, i.e., away from the emission maxima. Therefore, the intervals I_1 between 790.223 and 840.214 nm and I_2 between 840.214 and 945.344 nm were used in most cases. However, the intervals I_1 between 804.479 and 807.808 nm and I_2 between 871.774 nm and 877.045 nm were used when the fluorescence count was low, i.e., in the deep tissue configuration. The calibration with the compact spectrometer and the thermal camera led to $a = 1.524 \pm 0.025$, $b = -1.382 \pm 0.003 \text{ K}^{-1}$, and $a = 2.957 \pm 0.030$, $b = -1.843 \pm 0.003 \text{ K}^{-1}$ in the low count case. During the calibration, the temperature was changed either using a heating plate or by changing the laser power.

The fluorescence was collected to measure the temperature during soldering of pig intestine (external side on top; tissue thickness of 1–2 mm) using an integration time of 1–3 s. The signal was then presented using a moving average over two adjacent data points.

Feedback-Controlled Heating: A PID controller was used ($P = 0.01$, $I = 0.001$, $D = 0.005$) to modulate the laser power based on the signal measured by the portable NIR spectrometer in order to achieve a pre-set target temperature. A microcontroller (Arduino UNO) was used to control the laser output. The performance of the controller was tested on the solder paste and confirmed using as reference a thermal camera. The performance was tested both in a stationary case and when the fibers used for heating and sensing were moved to adjacent regions on the solder paste during soldering.

Water-Filtered Infrared (wIRA) Soldering: Porcine small intestine and pig liver were obtained from a local slaughterhouse on the same day of the experiment. Samples were cut into pieces having the desired shape using a surgical scissor or a scalpel and then placed on a transparent plexiglass surface. Pieces of the intestine were maintained at a low temperature and hydrated by spraying with PBS when necessary. Soldering was carried out with TiN-based solder paste (BSA 25%, gelatin 6.5%, TiN 0.01%, BiVO 0.3%) using a Hydrosun 750 placed 5 cm from the samples as an illumination source suitable for reaching the required soldering temperature. The samples were illuminated for 4 min and hydrated by spraying with PBS several times over the illumination period. Histological samples were then collected.

Histology Preparation: Samples were placed in formalin solution for at least 24 h before histological processing. The histology sectioning and H&E staining were carried out by a specialized external facility (Sophistolab AG, 4132 Muttenz, Switzerland) following standard histological procedures. Histological cuts were 3 μm thick. Images were acquired using a slide scanner (Pannoramic 250, 3DHISTECH).

Paste Stability in PBS and FaSSIF: Solder pastes with 25% BSA, 6.5% gelatin, 0.01% TiN, and 0.3% BiVO were prepared as described previously. The 750 nm laser illuminated the paste at full power for 4 min to prepare the soldered samples. Fasted state simulated intestinal fluid (FaSSIF) was prepared by adding 2.016 g of FaSSIF powder (Biorelevant Ltd) in a solution containing 37.48 g of FaSSIF buffer concentrate (Biorelevant Ltd.) and 865.0 g of distilled water. The solution was stirred until complete dissolution and equilibrated for 2 h before use. The pastes were weighed before immersing them in 25 mL of PBS or FaSSIF and afterward at various intervals. The pastes were dried with a microfiber tissue prior to weighing. Triplicates for each sample category were used.

Bacterial Leakage Experiment: Porcine small intestine and pig liver were obtained from a local slaughterhouse on the same day of the experiment, and 25 cm long pieces were prepared. Three categories of samples were prepared: intact, defective, and soldered, and three samples were prepared for each category. For the defective and soldered samples, a defect measuring ≈4 mm was created parallel to the intestine direction on its side. For the soldered samples, the defect was soldered using a TiN/BiVO paste (25% BSA, 6.5% gelatin, 0.01% TiN, 0.3% BiVO) and the 750 nm laser at full power for 4 min.

The extremities of the intestine pieces were clamped, and the samples were immersed in a flask containing 100 mL of LB broth, forming a “U” shape, with the extremities fixed at the flask’s rim. In each sample, 6 mL of LB broth containing *Escherichia coli* (*E. coli*) was poured inside. The *E. coli* K12 strain MG1655 with GFP controlled by the lambda phage promoter pR, inserted at the attB site, was used. The broth surrounding the intestines was collected and analyzed at the beginning, every hour, and after 24 h. For each sample, 300 μL were pipetted three times in a well plate, and the absorbance (at 492 ± 10 nm) and fluorescence (excitation: 485 ± 20 nm; emission: 535 ± 25 nm) were measured by a plate reader (Infinite F200 PRO, Tecan).

Burst Pressure Measurements: Porcine small intestine was obtained from a local slaughterhouse on the same day of the experiment. The intestine was cut open and flat, and a 1 cm cut parallel to the intestine length was created with surgical scissors to measure the burst pressure. The intestines were sutured using polypropylene sutures (Ethicon Prolene 5-0, the standard type and thickness of suture used for small bowel anastomoses in clinical practice). The intestines were soldered using a TiN/BiVO paste (BSA 25%, gelatin 6.5%, TiN 0.01%, BiVO 0.3%) and a 750 nm laser.

The intestine was mounted on a 3D-printed burst pressure apparatus created following the design criteria of Nam and Mooney^[51]. A pump (Lambda VIT-FIT) was used to fill the intestines with DI water at a rate of 1 mL min⁻¹. Triplicates were used for each sample group. A pressure sensor (ABPDANV060PGSA3, Honeywell) was connected to the apparatus to measure the burst pressure. Methylene blue (Sigma-Aldrich, 03978) was dispersed in water and used to check the suture and solder water-tightness visually.

In Vivo Soldering: An in vivo study was approved by the Commission of Work with Experimental Animals (project ID: MSMT-15629/2020-4) under the Czech Republic’s Ministry of Agriculture supervision. All procedures were carried out according to Czech and EU law.

A combined intramuscular injection of ketamine (Narkamon 100 mg mL⁻¹, BioVeta a.s., Ivanovice na Hané, Czech Republic) and azaperone (Stresnil 40 mg mL⁻¹, Elanco AH, Prague, Czech Republic) was used to pre-medicate a healthy female Prestice Black-Pied pig (3 months old). Continuous intravenous propofol injection (Propofol 2% MCT/LCT Fresenius Medical Care a.s.) was used to maintain general anesthesia. Nalbuphine (Nalbuphin, Torrex Chiesi CZ s.r.o., Czech Republic) was used intravenously for analgesia assurance.

The abdominal cavity was entered via a midline laparotomy. An end-to-end small intestine anastomosis was performed 50 cm aboral from the duodeno-jejunal transition. Additionally, end-to-end anastomoses were

performed on the ureter, the fallopian tube, and the renal vein. The anastomoses were sealed using the iSoldering approach (paste with BSA 25%, gelatin 6.5%, TiN 0.01%, BiVO 0.3% soldered with the 750 nm laser for 4 min).

After euthanasia, tissue samples were collected and chemically fixed in 4% paraformaldehyde in PBS. Histology samples were processed (embedded, sectioned, and stained) by SophistoLab, Muttenz, Switzerland. Samples were imaged using a whole slide scanner at ScopeM, ETH Zurich.

Mechanical Testing: Porcine small intestine and pig liver were obtained from a local slaughterhouse on the same day of the experiment. A water-based gravimetric tensile strength apparatus was used for tensile strength measurements with a constant loading increase of 39.2 mN s^{-1} .

Intestine samples were cut into rectangular pieces of 0.5–1 cm width with a full-width cut placed in the middle. Samples were soldered with solder pastes of various BSA, gelatin, and TiN concentrations within the defined ranges and using the 750 nm laser for up to 4 min at full or variable power. Failure was defined by the full separation of the specimen, whether or not it occurred at the weld site. Tensile strength was obtained from the breaking load normalized by the width of the weld. $N = 18$ for soldered samples and $N = 3$ for intact samples.

Statistical Analysis: No data preprocessing had been employed. Data in bar and line charts are displayed as mean \pm SD. The sample size (N) was indicated in the figure captions and Experimental Section. Matlab, Python, and Origin Pro had been used for data processing.

Supporting Information

Supporting Information is available from the Wiley Online Library or from the author.

Acknowledgements

The authors thank Dr. Arthur Shapiro and Prof. David Norris (OMEL, ETH Zurich) for access to UV–vis–NIR measurements. The authors thank Dr. Jose Garcia-Guirado and Prof. Romain Quidant (NSL, ETH Zurich) for access to the 1064 nm laser, Dr. Vera Kissling (Empa) for transmission electron microscopy, and Dr. Pascal Gschwend (ETH Zurich) for his support with nanothermometry. The authors thank Dr. Markus Arnoldini, Erica Facin, and Prof. Emma Slack (ETH Zurich) for their help with the bacterial experiments and Dr. Tobias Bergmiller (University of Exeter) for developing the bacteria strain. The authors acknowledge funding from the Swiss National Science Foundation (Eccellenza, 181290) and the Oertli Foundation, and thank the Erwin Braun Foundation for providing the WIRA lamp.

Open access funding provided by Eidgenössische Technische Hochschule Zurich.

Conflict of Interest

O.C. and I.K.H. declare inventorship on a patent application by ETH Zurich and Empa: Composition for Laser Tissue Soldering, EP21216014.7. All other authors declare no conflict of interest.

Data Availability Statement

The data that support the findings of this study are available from the corresponding author upon reasonable request.

Keywords

nanotechnology, surgery, suturing, thermoplasmonics, tissue sealing

Received: June 1, 2023

Revised: July 27, 2023

Published online:

- [1] S. E. Tevis, G. D. Kennedy, *J. Surg. Res.* **2013**, *181*, 106.
- [2] B. Bao, T. Gao, X. Li, H. Wei, J. Lin, Y. Sun, J. Shen, H. Zhu, X. Zheng, *Int J Surg* **2022**, *98*, 106214.
- [3] J. Wu, H. Yuk, T. L. Sarrafian, C. F. Guo, L. G. Griffiths, C. S. Nabzdyk, X. Zhao, *Sci. Transl. Med.* **2022**, *14*, eabh2857.
- [4] K. Zheng, Q. Gu, D. Zhou, M. Zhou, L. Zhang, *Smart Mater Med* **2022**, *3*, 41.
- [5] J. Hammond, S. Lim, Y. Wan, X. Gao, A. Patkar, *J Gastrointest Surg* **2014**, *18*, 1176.
- [6] A. H. C. Anthis, X. Hu, M. T. Matter, A. L. Neuer, K. Wei, A. A. Schlegel, F. H. L. Starsich, I. K. Herrmann, *Adv. Funct. Mater.* **2021**, *31*, 2007099.
- [7] A. H. C. Anthis, M. P. Abundo, A. L. Neuer, E. Tsolaki, J. Rosendorf, T. Rduch, F. H. L. Starsich, V. Liska, A. A. Schlegel, M. G. Shapiro, I. K. Herrmann, *Nat. Commun.* **2022**, *13*, 7311.
- [8] D. M. Toriumi, W. F. Raslan, M. Friedman, M. E. Tardy, *Arch Otolaryngol* **1990**, *116*, 546.
- [9] Y. Takegawa, T. Takao, H. Sakaguchi, T. Nakai, K. Takeo, Y. Morita, T. Toyonaga, Y. Kodama, *Sci. Rep.* **2022**, *12*, 6986.
- [10] A. P. Duarte, J. F. Coelho, J. C. Bordado, M. T. Cidade, M. H. Gil, *Prog. Polym. Sci.* **2012**, *37*, 1031.
- [11] H. Yuk, C. E. Varela, C. S. Nabzdyk, X. Mao, R. F. Padera, E. T. Roche, X. Zhao, *Nature* **2019**, *575*, 169.
- [12] B. Kong, R. Liu, Y. Cheng, Y. Shang, D. Zhang, H. Gu, Y. Zhao, W. Xu, *Adv. Sci.* **2022**, *9*, 2203096.
- [13] N. Annabi, K. Yue, A. Tamayol, A. Khademhosseini, *Biol. Barriers.* **2015**, *95*, 27.
- [14] R. Schober, F. Ulrich, T. Sander, H. Dürselen, S. Hessel, *Science* **1986**, *232*, 1421.
- [15] K. M. McNally, B. S. Sorg, A. J. Welch, J. M. Dawes, E. R. Owen, *Phys Med Biol* **1999**, *44*, 983.
- [16] P. Matteini, F. Rossi, F. Ratto, R. Pini, in *Laser Imaging and Manipulation in Cell Biology*, (Ed.: F. S. Pavone), John Wiley & Sons, Ltd, Hoboken, NJ **2010**, pp. 203–231.
- [17] D. F. Gomes, I. Galvão, M. A. R. Loja, *Appl. Sci.* **2019**, *9*, 2157.
- [18] A. Krisch, C. S. Cooper, J. Gatti, H. Scherz, D. Cannig, S. Zderic, H. M. Snyder III, *J Urol* **2001**, *165*, 574.
- [19] Y. A. Mistry, S. S. Natarajan, S. A. Ahuja, *Ann Maxillofac Surg* **2018**, *8*, 35.
- [20] J. Dong, H. Breitenborn, R. Piccoli, L. V. Besteiro, P. You, D. Caraffini, Z. M. Wang, A. O. Govorov, R. Naccache, F. Vetrone, L. Razzari, R. Morandotti, *Biomed Opt Express* **2020**, *11*, 2254.
- [21] D. R. Pabittei, W. de Boon, M. Heger, R. F. van Golen, R. Balm, D. A. Legemate, B. A. de Mol, *J. Clin. Transl. Res.* **2015**, *1*, 1.
- [22] D. Simhon, M. Halpern, T. Brosh, T. Vasilyev, A. Ravid, T. Tennenbaum, Z. Nevo, A. Katzir, *Ann. Surg.* **2007**, *245*, 206.
- [23] G. Esposito, F. Rossi, A. Puca, A. Albanese, G. Sabatino, P. Matteini, G. Lofrese, G. Maira, R. Pini, *J Biol Regul Homeost Agents* **2010**, *24*, 307.
- [24] M. E. Khosroshahi, M. S. Nourbakhsh, *J. Biomed. Opt.* **2011**, *16*, 088002.
- [25] P. K. Jain, K. S. Lee, I. H. El-Sayed, M. A. El-Sayed, *J Phys Chem B* **2006**, *110*, 7238.
- [26] M. Hu, J. Chen, Z.-Y. Li, L. Au, G. V. Hartland, X. Li, M. Marquez, Y. Xia, *Chem. Soc. Rev.* **2006**, *35*, 1084.
- [27] M. Mushaben, R. Urie, T. Flake, M. Jaffe, K. Rege, J. Heys, *Lasers Surg Med* **2018**, *50*, 143.
- [28] V. Sriramoju, H. Savage, A. Katz, R. Muthukattil, R. R. Alfano, *Lasers Surg Med* **2011**, *43*, 991.
- [29] P. Matteini, F. Ratto, F. Rossi, R. Pini, *J. Biomed. Opt.* **2012**, *17*, 010701.
- [30] G. Baffou, F. Cichos, R. Quidant, *Nat. Mater.* **2020**, *19*, 946.
- [31] H.-C. Huang, C. R. Walker, A. Nanda, K. Rege, *ACS Nano* **2013**, *7*, 2988.
- [32] L. S. Bass, M. R. Treat, *Lasers Surg Med* **1995**, *17*, 315.

- [33] J. Zhou, B. del Rosal, D. Jaque, S. Uchiyama, D. Jin, *Nat Methods* **2020**, *17*, 967.
- [34] D. Jaque, F. Vetrone, *Nanoscale*. **2012**, *4*, 4301.
- [35] L. M. Maestro, C. Jacinto, U. R. Silva, F. Vetrone, J. A. Capobianco, D. Jaque, J. G. Solé, *Small*. **2011**, *7*, 1774.
- [36] S. Li, K. Zhang, J.-M. Yang, L. Lin, H. Yang, *Nano Lett.* **2007**, *7*, 3102.
- [37] M. Umezawa, K. Nigoghossian, in *Transparency in Biology: Making the Invisible Visible*, (Eds.: K. Soga, M. Umezawa, K. Okubo), Springer, Singapore, **2021** pp. 139–166.
- [38] P. Haro-González, L. Martínez-Maestro, I. R. Martín, J. García-Solé, D. Jaque, *Small*. **2012**, *8*, 2652.
- [39] P. M. Gschwend, D. Niedbalka, L. R. H. Gerken, I. K. Herrmann, S. E. Pratsinis, *Adv. Sci.* **2020**, *7*, 2000370.
- [40] C. D. S. Brites, P. P. Lima, N. J. O. Silva, A. Millán, V. S. Amaral, F. Palacio, L. D. Carlos, *Nanoscale*. **2012**, *4*, 4799.
- [41] F. Vetrone, R. Naccache, A. Zamarrón, A. Juarranz de la Fuente, F. Sanz-Rodríguez, L. Martínez Maestro, E. Martín Rodríguez, D. Jaque, J. García Solé, J. A. Capobianco, *ACS Nano* **2010**, *4*, 3254.
- [42] S. Balabhadra, M. L. Debasu, C. D. Brites, L. A. Nunes, O. L. Malta, J. Rocha, M. Bettinelli, L. D. Carlos, *Nanoscale* **2015**, *7*, 17261.
- [43] S. Senapati, K. K. Nanda, *J. Mater. Chem. C*. **2017**, *5*, 1074.
- [44] P. M. Gschwend, S. Conti, A. Kaech, C. Maake, S. E. Pratsinis, *ACS Appl. Mater. Interfaces*. **2019**, *11*, 22550.
- [45] S. Bogni, D. Schöni, M. Constantinescu, A. Wirth, I. Vajtai, A. Bregy, A. Raabe, U. Pieleles, M. Frenz, M. Reinert, *Acta Neurochirurgica Supplementum*, (Eds.: T. Tsukahara, L. Regli, D. Hänggi, B. Turowski, H.-J. Steiger), Springer, Vienna **2011**, pp. 45–53.
- [46] P. M. Gschwend, F. H. L. Starsich, R. C. Keitel, S. E. Pratsinis, *Chem. Commun.* **2019**, *55*, 7147.
- [47] L. Sanders, J. Nagatomi, *Crit Rev Biomed Eng* **2014**, *42*, 271.
- [48] H. Suzuki, N. Kobayashi, T. Nagaoka, K. Iwasaki, M. Umezawa, S. Takeda, T. Togawa, in 2006 Int. Conf. of the IEEE Engineering in Medicine and Biology Society, IEEE, New York, NY, USA **2006**, pp. 799–802.
- [49] K. M. McNally, B. S. Sorg, N. C. Bhavaraju, M. G. Ducros, A. J. Welch, J. M. Dawes, *Appl. Opt.* **1999**, *38*, 6661.
- [50] R. L. Mcintosh, V. Anderson, *Biophys. Rev. Lett.* **2010**, *05*, 129.
- [51] S. Nam, D. Mooney, *Chem. Rev.* **2021**, *121*, 11336.